



Cite this: *Nanoscale*, 2025, **17**, 25691

## “In Rust we Shine”: an all-in-one photo-electrocatalytic device for low-cost infrared-induced water splitting with a hematite–polymeric EVA film containing rare-earth up-conversion particles

J. Méndez-Ramos,<sup>a</sup> A. Menéndez-Velázquez,<sup>\*c</sup> J. del-Castillo,<sup>b</sup> M. Medina-Alayón,<sup>a,b</sup> A. B. García-Delgado,<sup>c</sup> S. Torres-García,<sup>a,b</sup> P. Acosta-Mora,<sup>a,b</sup> M. E. Borges,<sup>d</sup> C. B. Mullins<sup>e</sup> and P. Esparza<sup>\*f</sup>

Handling and transforming solar radiation with spectral conversion luminescent materials constitute a frontier approach in photonic research for advancing environmental catalysis and sustainable hydrogen production *via* photocatalytic water splitting. In this study, a photon-assisted approach is used to enhance the photocatalytic activity of hematite ( $\alpha\text{-Fe}_2\text{O}_3$ ) photoelectrodes using  $\text{Yb}^{3+}$  and  $\text{Er}^{3+}$  co-doped  $\text{NaYF}_4$  particles. These particles emit intense green light through near infrared-to-visible up-conversion, with emission wavelengths well aligned with the bandgap of hematite, thereby optimizing photo-electrochemical water splitting. Moreover, luminescent ethylene vinyl acetate (EVA) films embedded with up-conversion particles were fabricated and utilized to manufacture laminated glass structures, with hematite coated on the opposite side. This all-in-one photonic device serves as a proof of concept for an industrially relevant platform enabling low-cost infrared-driven water splitting. Photocurrent generation in this system is driven exclusively by mainly green upconverted photons under excitation from a 980 nm diode laser, which are absorbed by the hematite layer. The resulting up-converted green light emitted from the EVA film triggers surface oxidation on the hematite photocatalyst, demonstrating that water splitting can be achieved through the up-conversion luminescence alone. Thus, we are proving that even with low energy green and red up-conversion emission, it is possible to enable up-conversion-driven water-splitting reactions.

Received 4th August 2025,  
Accepted 6th October 2025

DOI: 10.1039/d5nr03289j

rsc.li/nanoscale

## Introduction

The bio-inspiration of photosynthesis leads the way to renewable solar-driven hydrogen energy sources. Sunlight can be harnessed to rearrange the low-energy bonds of water into high-energy bonds of hydrogen and oxygen to store energy, much like the process carried out by chloroplasts in plants.<sup>1,2</sup> The utilization of the long infrared tail of incident solar radi-

ation has untapped and crucial applications in photocatalysis and energy harvesting schemes.<sup>3</sup> “There is plenty of energy at the bottom”, paraphrasing the revered Professor Feynman, which paves the way for harvesting the large infrared tail of incident irradiation from the Sun, aimed toward photocatalytic applications.<sup>4,5</sup> Handling and transforming incoming infrared radiation from the Sun (which accounts for more than 50% of solar energy) with up-conversion luminescent materials<sup>6</sup> constitutes a frontier approach in photonic research in pursuit of boosting hydrogen production *via* photocatalytic water splitting in photo-electrochemical cells (PECs).<sup>7</sup> Up-conversion luminescence processes act like a bridge over troubled gaps,<sup>8</sup> in this case, providing extra photons for absorption using catalysts to bridge the large bandgap of photocatalytic semiconductors as a not yet fully explored highway.

One of the most useful and interesting materials for photoelectrodes is hematite ( $\alpha\text{-Fe}_2\text{O}_3$ ), having garnered significant attention due to its abundance, low-cost, stability, non-toxic nature and its electronic band gap being suitable for efficient

<sup>a</sup>Departamento de Física, Universidad de La Laguna, Tenerife, Spain.

E-mail: jmendezr@ull.edu.es

<sup>b</sup>Instituto Universitario de Materiales y Nanotecnología, Universidad de La Laguna, Tenerife, Spain

<sup>c</sup>Unidad de Materiales Fotoactivos, Centro Tecnológico IDONIAL, 33417 Avilés, Asturias, Spain. E-mail: amador.menendez@idonial.com

<sup>d</sup>Departamento de Ingeniería Química, Universidad de La Laguna, Tenerife, Spain

<sup>e</sup>Department of Chemistry, Texas Materials Institute; McKetta Department of Chemical Engineering, The University of Texas at Austin, Austin, Texas 78712, USA

<sup>f</sup>Departamento de Química Inorgánica, Universidad de La Laguna, Tenerife, Spain. E-mail: pesparza@ull.edu.es



absorption of visible light in a photo-electrochemical cell (PEC).<sup>9,10</sup> Hematite has been identified as one of the most promising photoanode materials,<sup>11,12</sup> since its absorption range lies within the visible region up to around 610 nm,<sup>9</sup> which makes it an accurate candidate for solar energy conversion utilized in PEC water splitting.<sup>13,14</sup> Thus, to further improve its photocatalytic efficiency, up-conversion processes have become key factors when converting infrared radiation over the hematite absorption wavelength range. Incorporating rare-earth-doped materials for up-conversion, in particular, highly efficient Yb<sup>3+</sup>-Er<sup>3+</sup> co-doped NaYF<sub>4</sub> particles, will enable the absorption of near-infrared light, which is then re-emitted mainly as green photons.<sup>5,15</sup> These additional photons can be absorbed by hematite, thus improving its efficiency in the water-splitting process. Herein, we explore this potential approach to enhance hematite's performance in solar energy applications, absorbing near-infrared radiation and emitting in the visible range,<sup>16</sup> so that more photons can be provided for absorption by hematite photoelectrodes for water splitting.<sup>9,12,17</sup> Our approach can shed light on the state of the art of up-conversion-sensitized photocatalysis since, in the last few years, there has been an increasing number of published works where the up-conversion effect is largely assumed, and unfortunately misinterpreted in many cases, as pointed out by Prof. Cates and co-workers in ref. 18, rather than proven experimentally.<sup>19,20</sup> In this work, we emphasize the sole role of the photonic up-conversion effect in infrared-driven-boosted photocatalytic reactions, disregarding any possible side effects.<sup>5,8</sup> A 980 nm laser has been used as the only excitation source for achieving PEC water splitting. This set-up proves that activation of an  $\alpha$ -Fe<sub>2</sub>O<sub>3</sub> photocatalyst occurs only under NIR irradiation up-converted into suitable green photons. Thus, we present the role of a solely up-conversion luminescence effect to split water over a hematite photoelectrode: "in rust we shine".

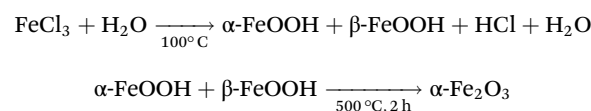
Also, in this work, we present a quite significant added value, which is related to the integration method of our up-conversion agent, solvothermal NaYF<sub>4</sub>:Yb<sup>3+</sup>,Er<sup>3+</sup> micro-sized particles,<sup>21</sup> within the PEC set-up and the hematite photoelectrode. In detail, an ethylene vinyl acetate (EVA) thermoplastic copolymer film has been doped with up-conversion particles, forming luminescent EVA layers. These layers were then used to manufacture laminated glass, with hematite coated on the opposite side. EVA is widely recognized for its excellent optical and mechanical properties and is commonly used in conventional silicon and thin-film photovoltaic (PV) solar cells as a protective polymer layer that shields against environmental degradation, particularly from moisture.<sup>22</sup> At the same time, EVA has high transmittance in the visible/NIR region of the spectrum, ensuring that it does not block sunlight that would otherwise reach the solar cells. These attributes are crucial to the objectives of this study. First, EVA's resistance to moisture enables its application in aquatic or humid environments. Second, its high transmittance in the visible-NIR range minimizes parasitic absorption of both incoming NIR light and up-converted visible emission. In addition, EVA offers excellent

chemical and optical compatibility as a host matrix for luminescent species, maintaining—or at least not significantly quenching—their luminescence properties during the transition from solution to the solid state.<sup>23</sup> In particular, the EVA polymer demonstrated good compatibility with the luminescent agent investigated in this work. Overall, the use of EVA in this system represents a proof of concept of this all-in-one photonic device for low-cost infrared-induced hydrogen generation *via* water splitting.

## Experimental

### Hematite ( $\alpha$ -Fe<sub>2</sub>O<sub>3</sub>) photoanode preparation

The synthesis procedure consists of growing a well-ordered and oriented iron oxide nanorod layer onto a transparent conducting polycrystalline substrate to study its optical and photo-electrochemical properties. The growth of the three-dimensional array of crystalline highly oriented hematite nanorod bundles was conducted according to ref. 24. The preparation was performed with reagent grade chemicals. An aqueous solution (Milli Q water) of 0.15 M ferric chloride (FeCl<sub>3</sub>·6H<sub>2</sub>O, Scharlau 99%) and 1M sodium nitrate (NaNO<sub>3</sub>, Scharlau 99%) containing a polycrystalline FTO substrate (F-SnO<sub>2</sub>) (1.1 mm thickness, 7  $\Omega$  cm<sup>-2</sup>) was heated in an autoclave by following a hydrothermal synthesis method at a constant temperature of 100 °C for 5 h. Subsequently, the thin films formed were thoroughly washed with water to remove any residual salts. A second heat treatment in air at 500 °C for 2 h was performed to obtain a pure translucent brown thin film, which comprises the thermodynamically stable crystallographic phase of ferric oxide ( $\alpha$ -Fe<sub>2</sub>O<sub>3</sub>). An in-depth description of the preparation of the photoanode is presented in the SI:



### Synthesis of solvothermal NaYF<sub>4</sub>:Yb<sup>3+</sup>,Er<sup>3+</sup> up-conversion micro-sized particles

Micro-sized particles with composition NaY<sub>0.93</sub>Yb<sub>0.05</sub>Er<sub>0.02</sub>F<sub>4</sub> were obtained by the solvothermal method described as follows.<sup>25</sup> Oleic acid (90%), erbium acetate ((CH<sub>3</sub>COO)<sub>3</sub>Er, 99.9%), yttrium acetate ((CH<sub>3</sub>COO)<sub>3</sub>Y, 99.9%), ytterbium(III) chloride hexahydrate (YbCl<sub>3</sub>·6H<sub>2</sub>O, 99.998%), sodium hydroxide (NaOH, 97%), ammonium fluoride (NH<sub>4</sub>F, 98%) and ethanol (anhydrous) were purchased from Sigma-Aldrich and used as received. Briefly, a transparent homogeneous solution was obtained by vigorous stirring of a 2 ml aqueous solution containing 0.3 g of NaOH, 10 ml of ethanol and 20 ml of oleic acid. Next, a 2 ml aqueous solution containing 0.485 mmol of Y(CH<sub>3</sub>COO)<sub>3</sub>, 0.025 mmol of YbCl<sub>3</sub>·6H<sub>2</sub>O and 0.01 mmol of Er(CH<sub>3</sub>COO)<sub>3</sub>·H<sub>2</sub>O was added to the above solution. Finally, a 2 ml aqueous solution containing 2 mmol of NH<sub>4</sub>F was added, and after stirring for about 30 min, the as-obtained homo-



geneous colloidal solution was transferred into a 50 ml stainless Teflon-lined autoclave, sealed, and kept at 220 °C for 24 h. The autoclave was naturally cooled down to room temperature. The precipitate deposited at the bottom of the Teflon vessel was collected by centrifugation. Then, it was washed twice by re-dispersing in 4 ml of cyclohexane, followed by precipitation with 8 ml of ethanol. Finally, it was recovered using centrifugation and air-dried at 60 °C for 12 h.

### Fabrication of luminescent and non-luminescent EVA films followed by glass lamination

This section outlines the fabrication of luminescent ethylene vinyl acetate (EVA) films doped with different NaYF<sub>4</sub> up-conversion particles and non-luminescent EVA films, followed by glass lamination.

Initially, EVA pellets were dissolved in toluene under constant stirring at 80 °C until complete dissolution was achieved. The NaYF<sub>4</sub> up-conversion particle powder was then added to the solution, followed by vigorous mixing to ensure homogeneous dispersion. The resulting mixture contained different amounts of rare-earth-doped NaYF<sub>4</sub> particles: 2.5, 5 and 10 wt%, calculated relative to the EVA content.

Once the uniform dispersion had been obtained, the solvent was evaporated to yield solid EVA films doped with NaYF<sub>4</sub> particles. These films were then processed using a hot-plate press, applying controlled pressure and temperature to ensure uniformity produce films of varying thickness. The optimal configuration comprised EVA films containing 5 wt% NaYF<sub>4</sub> particles with a thickness of 1 mm, as will be proved in the following section.

In parallel, control (non-luminescent) EVA films were prepared using the same method, serving as reference samples for subsequent optical characterization studies.

All EVA films were subsequently used in the fabrication of laminated glass structures, with a hematite coating on the opposite side of the glass. Glass substrates were laminated, each incorporating a specific type of luminescent EVA film that covered only a portion of the glass surface. The remaining area was laminated with undoped EVA, serving as a reference for comparative optical characterization. The lamination process was carried out at an optimized temperature of 90 °C and a pressure of approximately 700 mbar, ensuring strong adhesion while preventing thermal degradation of the EVA matrix, the luminescent particles, and the hematite coating.

A 3-D infographic schematic model of our envisaged approach aimed at water splitting using hematite assisted by up-conversion luminescence, “in rust we shine”, is depicted in Fig. 1. Moreover, a schematic illustration of the preparation process of luminescent EVA films is presented in Fig. 2, along with photographs of the actual compact device comprising hematite photoelectrodes laminated with the luminescent EVA film, showing intense green up-conversion emission due to the rare-earth-doped NaYF<sub>4</sub> particles under excitation with a 980 nm laser. It should be noticed that the particles are intrinsically luminescent in their solid (powder) form. When introduced into a liquid medium, the particles do not dissolve but

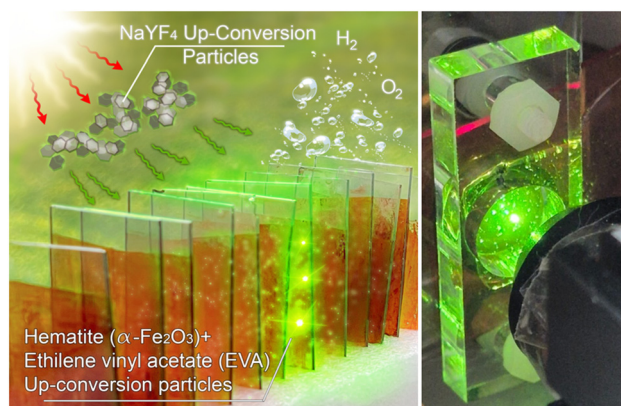


Fig. 1 A 3D infographic model of the envisaged approach aimed at water splitting using hematite assisted by up-conversion luminescence, “in rust we shine”, along with photographs of the luminescent EVA film laminated over the hematite photoelectrode.

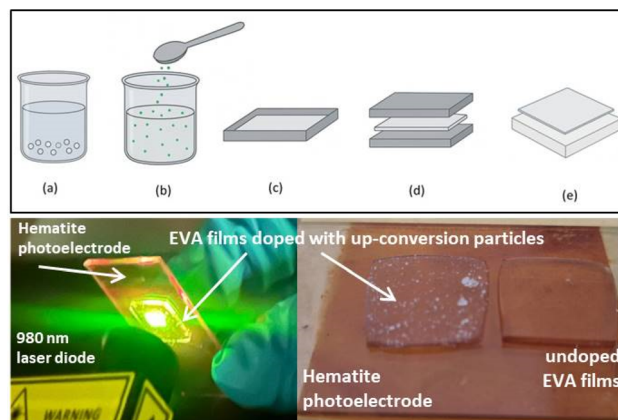


Fig. 2 Schematic illustration of the preparation process of luminescent EVA films. Upper images: (a) dissolution of EVA pellets in toluene; (b) addition of up-conversion particles to the EVA solution and their dispersion; (c) formation of luminescent EVA layers via the solvent casting process; (d) final luminescent EVA layers obtained through hot-pressing; and (e) glass laminated with the luminescent EVA layer. Lower images: photographs showing intense green up-conversion under excitation with an NIR 980 nm laser diode generated from the rare-earth-doped NaYF<sub>4</sub> particles embedded in the EVA films, as an all-in-one photonic device.

rather form a dispersion. In this dispersed state, they maintain their individual integrity and optical properties, and their photoluminescence is largely preserved due to the absence of strong interparticle interactions or aggregation that could lead to quenching mechanisms. After the film formation via solvent casting, the particles transition back into the solid state while being embedded within the host matrix. In this process, they essentially recover their original solid-state configuration, where they are again spatially isolated as in the initial powder form. Crucially, there is no chemical interaction or significant physical perturbation between the particles and the surrounding matrix material that could alter their emissive



properties. The matrix acts as a passive medium and does not introduce pathways for non-radiative decay. To support this assumption, we compared the emission properties of the solid microparticles in solution and when embedded in the EVA polymer after the casting process (see Fig. S1 in the SI). As it can be clearly seen, the emission profiles are identical, demonstrating that the EVA polymer matrix acts as a passive medium and does not interfere with the intrinsic luminescence of the microparticles.

### Up-conversion luminescence characterization

Up-conversion measurements were carried out using a continuous wave infrared collimated laser diode at 980 nm with a power of up to 300 mW and focused onto the sample using a 4× micro-objective, with a focal length of 4.51 mm and a numerical aperture of 0.55, which led to a micron-size area for the laser spot over the sample and therefore with a very intense power density.<sup>4,5</sup> Detection was carried out with a 0.25 m monochromator equipped with a photomultiplier tube. A 4× microscope objective lens was used for concentrating incident laser radiation onto the samples. All spectra were collected at room temperature and corrected for instrumental response.

### Structural characterization

XRD measurements were carried out using a Philips Panalytical X'Pert Pro diffractometer (with a primary monochromator, a Cu K $\alpha$ 1 radiation source ( $\lambda = 1.5406 \text{ \AA}$ ) and an X'Celerator detector). XRD patterns were recorded with steps of 0.016° in the 2 $\theta$  angular range (10–80°) over a period of 30 min. The diffraction pattern of LaB<sub>6</sub> was used as an internal standard to calibrate the parameters of the instrumental profile. For NaYF<sub>4</sub> particles, TEM images were obtained and EDS measurements were conducted using a transmission electron microscope (JEOL-JEM 1400), with a field emission gun, operating at 100 kV and a point-to-point resolution of 0.44 nm.

The analyzed samples were prepared in acetone and finally dropped onto carbon-coated copper grids. The microstructure of the  $\alpha$ -Fe<sub>2</sub>O<sub>3</sub> photoanode was examined by scanning electron microscopy (SEM) (ZEISS EVO 15) operating at 200 kV. The equipment used an Oxford Link detector to perform energy-dispersive X-ray spectroscopy analysis (EDX, Oxford X-MAX). The corresponding UV–vis spectra were recorded using a UV–vis spectrometer (Varian Cary 3 UV–vis spectrometer) equipped with an integration sphere. The spectra were recorded in diffuse reflectance mode and transformed to Kubelka–Munk units.

### Up-conversion powered photo-electrochemical (PEC) cell set-up

The experimental set-up of the photo-electrochemical (PEC) cell used in this work comprised a quartz-made container with a specific shape holding three electrodes (working electrode, counter electrode, and reference electrode) submerged in an electrolyte.<sup>5,7</sup> The working electrode (photoanode) was  $\alpha$ -Fe<sub>2</sub>O<sub>3</sub> on FTO glass with an exposed surface area of 0.38 cm<sup>2</sup>. The counter electrode was a platinum spiral thread that produces hydrogen gas (H<sub>2</sub>). The reference electrode was made of silver/

silver chloride (Ag/AgCl) in a saturated solution of potassium chloride (KCl). When light strikes the surface of this semiconductor, it excites electrons from the valence band to the conduction band, creating electron–hole pairs, and the electrons are transferred to the electrolyte while the holes remain in the photoelectrode. The electrolyte used in this process is typically a solution of potassium hydroxide (in this case, a 1M KOH solution), which acts as a conductive medium between the anode and the cathode. The alkaline KOH solution also serves as a source of OH<sup>−</sup>, which are transformed into O<sub>2</sub> at the photoanode, producing the necessary electrons to induce hydrogen generation at the cathode. The counter electrode completes the circuit and allows the flow of electrons, resulting in the generation of an electrical current. A potentiostat (AMEL System 5000) was connected to the PEC cell to measure the obtained photocurrent, which was recorded. Measured potentials *versus* the reference are referred to the reversible hydrogen electrode (RHE), which is given by:

$$E(\text{vs. RHE}) = E(\text{vs. Ag/AgCl}_{\text{sat}}) + E^{\circ} \text{Ag/AgCl}_{\text{sat}} + 00591 \times \text{pH}$$

A constant anodic potential of 0.21 V *vs.* Ag/AgCl<sub>sat</sub> (meaning 1.23 V *vs.* RHE with alkaline pH 14, being  $E^{\circ} \text{Ag/AgCl}_{\text{sat}} = 0.197 \text{ V}$ ) was applied.

Under standard conditions, water can be electrolysed with an electrical potential of 1.23 V *vs.* RHE. The reaction in a PEC cell<sup>7</sup> can be summarized as  $\text{H}_2\text{O} + h\nu \rightarrow \text{H}_2 + \frac{1}{2}\text{O}_2$ . The electrochemical decomposition of water can only occur when the potential gap  $\Delta E \geq 1.23 \text{ eV}$ , so it will take place only when the energy of the absorbed incident photon on the photoelectrode surface is equal to or greater than that potential. In alkaline solution, the overall water-splitting reaction consists of two half reactions: the oxygen evolution reaction (OER) and the hydrogen evolution reaction (HER):



The anodic photocurrent is measured as the result of the OER. Photoelectrolysis was carried out using a 980 nm laser diode with a power value of up to 300 mW focused onto the sample using a 4× microscope objective lens.

## Results and discussion

### Structural characterization

First, we present a detailed structural characterization of the backbone of the photo-electrochemical set-up, that is, the hematite ( $\alpha$ -Fe<sub>2</sub>O<sub>3</sub>) photoanode, as shown in the SI. Fig. S2 in the SI shows the scanning electron microscopy (SEM) images of the synthesized ( $\alpha$ -Fe<sub>2</sub>O<sub>3</sub>) photoanode, showing a homogeneous hematite layer formed by an oriented structure of nanorods of about 50 nm in diameter. Fig. S1 also shows the cross-sectional image, indicating the mean thickness of the thin films of about 1.4  $\mu\text{m}$ . EDX spectra of the synthesized samples reveal that all samples are composed of Fe, Sn, O and a small amount of Si elements. The corresponding inset table



in Fig. S2 shows the atomic elemental composition. Accordingly, the sample is formed by hematite ( $\alpha\text{-Fe}_2\text{O}_3$ ) on the  $\text{SnO}_2$  film surface. The small amount of Si detected corresponds to the  $\text{SiO}_2$  glass substrate. Finally, the X-ray diffraction (XRD) pattern of a film of  $\alpha\text{-Fe}_2\text{O}_3$  grown onto a conducting F-SnO<sub>2</sub> glass substrate was recorded. The diffractograms obtained show that the chemical composition of the crystalline film corresponds to  $\alpha\text{-Fe}_2\text{O}_3$  (hematite) with a pure rhombohedral crystal structure<sup>24</sup> and  $\text{SnO}_2$  (cassiterite). Additional data including diffraction angles, and assignments of phases and planes to each peak are also presented in the SI, Table S1. The UV-vis absorption spectra of the  $\alpha\text{-Fe}_2\text{O}_3$  photoanode were also recorded, revealing that it absorbs radiation in the visible region below 650 nm (see Fig. S3 in the SI). The translucent brown thin films exhibited very strong absorbance, very close to 1 (100% of the light absorbed), in the range of 300–525 nm, followed by a monotonic linear decrease to 0.5 at 650 nm. The absorbance slowly decreased to 0.4 at 800 nm (40% of the light absorbed) but did not reach zero, most probably originating from multiple absorption phenomena within the nano-composite or scattering at the substrate interface. The total reflectance remained at a very low level (5%) within the whole wavelength range investigated, revealing very small amounts of light scattering by the film.

Next, we present a complete characterization study of the up-conversion agent used in our photonic approach, that is, solvothermal  $\text{NaYF}_4\text{:Yb}^{3+},\text{Er}^{3+}$  up-conversion micro-sized particles. The crystalline structure, size and distribution of the  $\text{NaYF}_4$  particles, as well as the influence of the synthesis methods used, were examined through XRD patterns and TEM images. Thus, Fig. 3 (lower image) shows the XRD pattern of solvothermal microparticles, in which well-defined diffraction peaks corresponding to hexagonal  $\text{NaYF}_4$  (JCPDS 28-1192) without impurities were observed. It can be clearly seen how diffraction peaks are shifted to higher angles according to different ionic radii ( $\text{Yb}^{3+}$  0.985 Å,  $\text{Er}^{3+}$  1.004 Å and  $\text{Y}^{3+}$  1.019 Å), supporting the successful incorporation of dopant ions into crystalline environments. The morphologies of  $\text{NaYF}_4$ -based materials were also analysed using TEM images (see Fig. 3, upper images). Micro-sized cylindrical-shaped particles with relatively broad size distribution are observed, with the average width and height being around 0.45  $\mu\text{m}$  and 1.3  $\mu\text{m}$ , respectively, as can be extracted from the corresponding histogram (see the inset in Fig. 3).

### Up-conversion luminescence

Up-conversion mechanisms are the cornerstone to enabling photocatalytic activity in hematite under infrared excitation by way of spectral shifting processes. Thus, as shown in Fig. 4, we present the up-conversion emission spectrum of solvothermal  $\text{NaYF}_4\text{:Yb}^{3+},\text{Er}^{3+}$  micro-sized particles. The up-converting particles absorb photons in the unused NIR range and emit intense visible radiation that can be absorbed by the hematite to induce photocatalysis. As it can be clearly seen, up-conversion emission bands within 410–660 nm perfectly match the hematite absorption also presented in Fig. S3 in the SI.

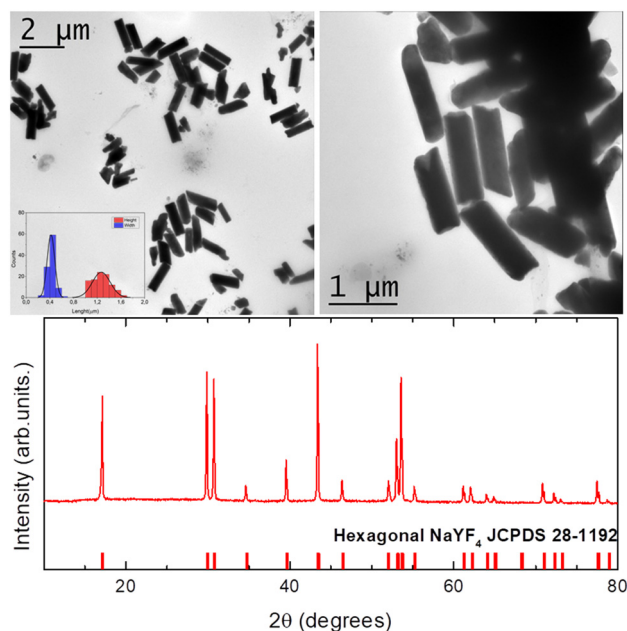


**Fig. 3** (top) Transmission electron microscopy (TEM) images of  $\text{NaYF}_4\text{:5\%Yb}^{3+}\text{-2\%Er}^{3+}$  micro-sized particles. Corresponding inset shows the particle size-distribution histograms. (bottom) XRD pattern of solvothermal  $\text{NaYF}_4\text{:5\%Yb}^{3+}\text{-2\%Er}^{3+}$  micro-sized particles with the standard data of hexagonal  $\beta\text{-NaYF}_4$ , JCPDS 28-1192.

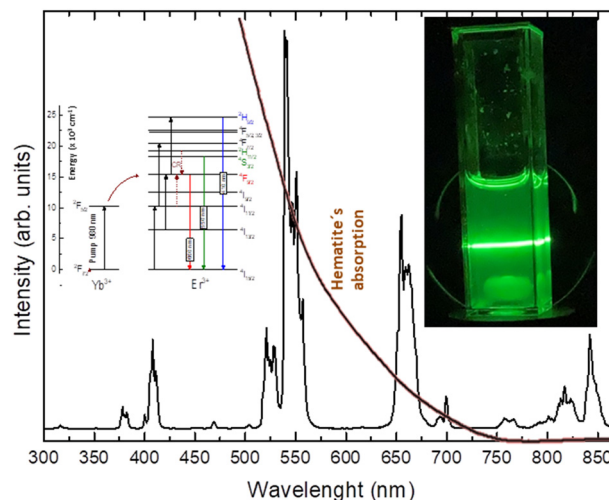


**Fig. 4** Up-conversion emission spectrum of solvothermal  $\text{NaYF}_4\text{:5\%Yb}^{3+}\text{-2\%Er}^{3+}$  micro-sized particles under excitation with a 980 nm laser diode with a power of up to 300 mW. The inset shows the energy level diagrams of  $\text{Yb}^{3+}$  and  $\text{Er}^{3+}$  ions with the main emission transitions labelled with the corresponding wavelengths. Also shown is a photograph of up-conversion solvothermal microparticles under infrared excitation. Hematite's absorbance curve is depicted by a red solid line as a reference to demonstrate the perfect overlap with the green up-conversion emission spectrum from the rare-earth-doped  $\text{NaYF}_4$  particles.

According to well-known energy transfer up-conversion mechanisms,<sup>3–6</sup> 980 nm NIR photons are efficiently absorbed by  $\text{Yb}^{3+}$  ions and the absorbed energy is sequentially trans-



ferred to  $\text{Er}^{3+}$  ions, which give rise to red, green and blue emissions located at 660, 550 and 410 nm, respectively (see the energy level diagrams in the inset of Fig. 4). The large absorption cross-section of  $\text{Yb}^{3+}$  ions at around 980 nm ( $^2\text{F}_{7/2} \rightarrow ^2\text{F}_{5/2}$  transition) is used as an efficient infrared antenna, resonant with many inexpensive NIR commercial laser diodes.

Therefore, “up-converted” photons in the visible range can activate  $\alpha\text{-Fe}_2\text{O}_3$  photocatalysts by generating electron-hole pairs to overcome the corresponding bandgap. An image of the  $\text{NaYF}_4:\text{Yb}^{3+},\text{Er}^{3+}/\text{NaYF}_4$  micro-sized particles emitting quite intense (as seen with the naked eye) bright green up-conversion luminescence under a 980 nm infrared pump is also presented in Fig. 4.

It is well known that photoluminescence is not a linear process with respect to dopant or particle concentration. Instead, the emission intensity typically increases until reaching an optimal concentration of dopant, beyond which it decreases due to different effects. To determine the optimum loading in our system, we systematically prepared and characterized samples with different microparticle concentrations. This approach allowed us to identify the concentration range that maximizes the up-conversion emission while minimizing detrimental effects. The performances of different concentrations of solvothermal  $\text{NaYF}_4:\text{Yb}^{3+},\text{Er}^{3+}$  particles embedded in the EVA film are presented, specifically for 2.5, 5 and 10% concentrations by weight (see Fig. 5). A straightforward luminescence comparison between the samples leads us to the selection of EVA films containing 5 wt%  $\text{NaYF}_4$  particles as the most efficient luminescent sample, and therefore this will be used in up-conversion-driven photocatalytic water splitting presented in the following section. At 10% concentration, the microparticles form aggregates within the EVA matrix, which increases optical scattering and creates local shadowing. This

reduces the effective excitation volume, as some particles shield others from the incident NIR light. In addition, the reduced interparticle distance can promote cross-relaxation processes between activator ions, leading to a further decrease in emission efficiency. Similar effects have been reported in the literature for up-conversion materials at high concentrations.<sup>26–28</sup>

At this point, it should be remarked that there is a full transmittance of the bare EVA polymer within the visible and NIR regions of the spectrum (only with high absorption in the UV range below 250 nm), as shown in Fig. S4 in the SI. Therefore, the EVA film does not interfere with green and red up-conversion emissions of the  $\text{NaYF}_4$  particles.

### Up-conversion powered water splitting by hematite

To demonstrate the actual ability of up-conversion luminescence to facilitate infrared-induced water splitting, we provide evidence of up-conversion-driven photocatalytic activity of  $\alpha\text{-Fe}_2\text{O}_3$  yielding hydrogen generation. For this purpose, we performed photo-electrocatalysis experiments with an original set-up of a Fujishima–Honda cell,<sup>5,7</sup> comprising the synthesized hematite ( $\alpha\text{-Fe}_2\text{O}_3$ ) photoanode aimed at measuring photoanodic currents.

Fig. 6 shows the current density obtained when IR light, from a 980 nm laser diode, is focused on the luminescent EVA film, containing solvothermal  $\text{NaYF}_4:\text{Yb}^{3+},\text{Er}^{3+}/\text{NaYF}_4$  micro-sized particles, which is laminated over the hematite photoelectrode in our PEC set-up for multi-cycle photoanodic current measurements. The detection of photocurrent generated when a 980 nm laser is turned on, as can be clearly seen in a single cycle in the inset of Fig. 6b, labelled as “UPCON booster”, confirms the generation of the required electron-hole pairs, and the subsequent water-splitting reaction, completely driven by up-converted photons. The incident 980 nm laser light by itself would be unable to activate the semiconductor without these spectral conversion processes. In detail, the mechanism works as follows: the intense green emitted radiation generated from the  $\text{NaYF}_4$  particles embedded in the EVA film under NIR excitation leads to oxidation on the  $\alpha\text{-Fe}_2\text{O}_3$  photocatalyst surface due to the perfect overlap of intense visible up-conversion emission bands (from 410 to 660 nm) and hematite absorbance (see Fig. 4). This spectral overlap will surpass the bandgap of the  $\alpha\text{-Fe}_2\text{O}_3$ , enabling water splitting and hydrogen generation. Thus, we obtained an “infrared-driven” straightforward activation of the  $\alpha\text{-Fe}_2\text{O}_3$  photoanode in a Fujishima–Honda PEC cell set-up<sup>5,7</sup> (see Fig. 6a). The photocurrent was measured using a potentiostat taking into account that the exposed surface of the photoelectrode is  $0.38\text{ cm}^2$ , as stated in the Experimental section. It should also be taken into account that when the light is switched on, photogenerated holes accumulate in the surface states, and when it is switched off, these trapped charges and intermediates discharge, leading to transient current peaks.<sup>29</sup> Moreover, the photocurrent follows a decay pattern that is inversely proportional to the square root of time, according to Cottrell’s equation.<sup>30</sup> Nevertheless, the results of single-cycle

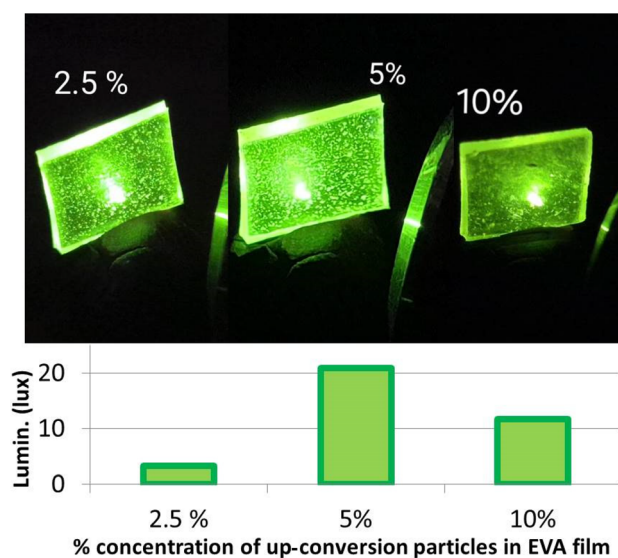
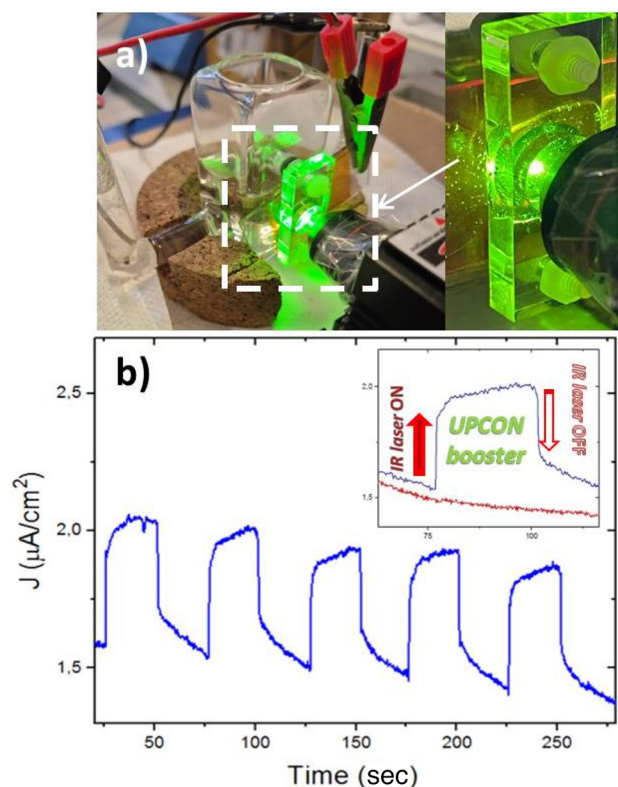


Fig. 5 Performance comparison of different concentrations of solvothermal  $\text{NaYF}_4:\text{Yb}^{3+},\text{Er}^{3+}$  particles embedded in the EVA film, for 2.5, 5 and 10% concentrations by weight.





**Fig. 6** (a) Photographs of the set-up of the up-conversion-powered PEC cell and detail of the luminescent EVA film containing rare-earth-doped  $\text{NaYF}_4$  particles, laminated over the hematite photoelectrode under 980 nm laser excitation. (b) Multi-cycle photoanodic current measurements obtained with a low-power NIR laser diode (980 nm) excitation source using the solvothermal  $\text{NaYF}_4:5\%\text{Yb}^{3+}-2\%\text{Er}^{3+}$  micro-sized particles as an up-conversion agent. The inset shows a single-cycle experiment along with the zero line (red curve) representing the null observed photocurrent in the absence of up-conversion particles.

and the multi-cycle experiments presented in Fig. 6b reveal a similar reaction profile, corresponding to a stationary regime.

The water-splitting reaction is only active while the infrared laser is switched on, and the photocurrent decreases to zero when the IR source is switched off, giving rise to significant photoanodic currents with use of only a single low-power IR excitation source (300 mW). This opens the way for indoor applications of photocatalytic processes using low-power and low-cost infrared laser diodes, instead of relatively expensive and harmful UV sources.<sup>31</sup> Moreover, the photocurrent measurements are not only shown for a single irradiation cycle, but multiple cycles are also included, as shown in Fig. 6b. It should be noted that the obtained values of the infrared-driven photocurrent presented here can be even higher, since the configuration of our set-up can be further optimized with future designs considering the wave-guiding of light into the PEC cell.<sup>4,5</sup>

On the other hand, we have disregarded the activation of  $\alpha\text{-Fe}_2\text{O}_3$  photocatalysts by any other unforeseen effect of the NIR light or by other thermal effects caused by possible

heating due to NIR laser irradiation.<sup>5,18</sup> In particular, in a control experiment, when focusing an NIR laser diode onto non-luminescent EVA films, where up-conversion  $\text{NaYF}_4$  particles were absent, no photocurrent was detected (see the zero line in the inset of Fig. 6b), evidencing that no hydrogen/oxygen evolution originated without up-conversion  $\text{NaYF}_4$  particles.

These control checks should never be underestimated to avoid misinterpretation of up-conversion-sensitized photocatalysis, extensively pointed out in detail by E. L. Cates and co-workers in ref. 18. In other words, in many recent works, the up-conversion effect in photochemistry is largely assumed rather than proven experimentally therein.<sup>18</sup> These control experiments, for example, using host materials without any up-conversion agent, are crucial to differentiate between optical or chemical effects.

For that reason, up-conversion-driven photocatalysis is here verified as a sole and unequivocally photonic effect, converting incident NIR radiation before reaching the solution reactor.<sup>5</sup>

Finally, in order to complete the photoelectrochemical characterization of the presented up-conversion-powered PEC cell,  $J$ - $V$  (current-voltage) curves are also shown in Fig. 7 using samples with and without the up-conversion particles embedded in the EVA film. It can be clearly observed the effect of light coming from the rare-earth-doped up-converting particles embedded in the EVA film (blue curve in Fig. 7) when comparing with the EVA film alone without the up-conversion particles (red curve in Fig. 7). The photocurrent is noticeably enhanced by the effect of up-conversion emission under excitation with a 980 nm laser diode, *i.e.*, the blue curve *vs.* the red curve in the  $J$ - $V$  (current-voltage) plot presented in Fig. 7.

Thus, harnessing infrared radiation holds promising potential for the activation of hematite photocatalysts. As the only

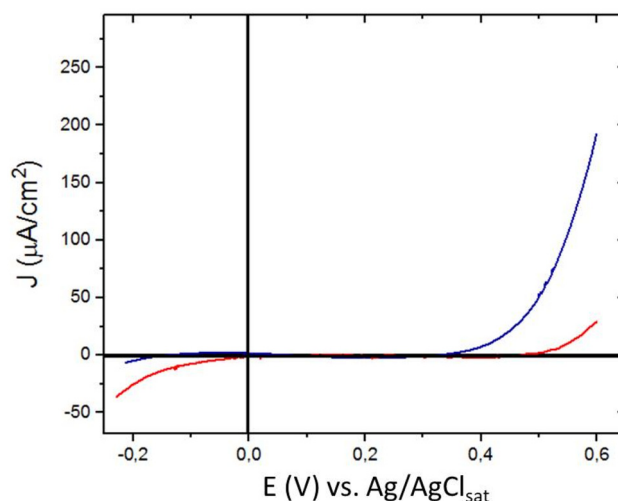


**Fig. 7**  $J$ - $V$  (current-voltage) curves at  $5 \text{ mV s}^{-1}$ , *i.e.*,  $J$  ( $\mu\text{A cm}^{-2}$ ) plotted against  $E$  (volts) vs.  $\text{Ag}/\text{AgCl}_{\text{sat}}$  under excitation with a 300 mW, 980 nm laser diode striking the rare-earth-doped up-converting particles embedded in the EVA film (blue curve) and striking the EVA alone without the up-conversion particles (red curve).



light to which the  $\alpha\text{-Fe}_2\text{O}_3$  surface is exposed is the 980 nm laser, we can ensure that only green up-converted photons are responsible in a pure photonic approach to the problem.<sup>5</sup> The incident NIR radiation is converted before it reaches the chemically unmodified  $\alpha\text{-Fe}_2\text{O}_3$  photocatalyst. This evidences the pure role of the photonic up-conversion effect in the NIR-driven water splitting utilizing hematite.

## Conclusions

Herein, we have proved an up-conversion-assisted activation of hematite photocatalysts using rare-earth-doped  $\text{NaYF}_4$  particles embedded into a polymeric EVA film using a simple original Fujishima and Honda PEC cell set-up. We have made use of one of the most useful, abundant and low-cost photoelectrode materials, that is, hematite ( $\alpha\text{-Fe}_2\text{O}_3$ ). Intense green up-conversion luminescence under 980 nm irradiation has led to the generation of a photoanodic current, which confirms the photochemical water-splitting reaction on the  $\alpha\text{-Fe}_2\text{O}_3$  surface, as a solely up-conversion luminescence effect to split water over a hematite photoelectrode: “in rust we shine”. Moreover, the successful integration of up-converting micro-sized rare-earth-doped  $\text{NaYF}_4$  particles into luminescent EVA films, which are used to laminate glass with hematite coated on the opposite side, represents a proof-of-concept approach and opens the way for indoor applications of this all-in-one photonic device.

## Conflicts of interest

There are no conflicts to declare.

## Data availability

The data supporting this article have been included as part of the supplementary information (SI). Supplementary information is available. See DOI: <https://doi.org/10.1039/d5nr03289j>.

## Acknowledgements

This work was financially supported by the MAGEC-REEsearch project (ProID2017010078) of “Agencia Canaria de Investigación” (ACIISI) and by Gobierno de Canarias (Proyecto “Tierras raras”, Grant Number SD- 22/25). It was also funded by FICYT – Consejería de Ciencia, Innovación y Universidad – Gobierno del Principado de Asturias through the 2018–2022 Science, Technology and Innovation Plan and by the European Union through the European Regional Development Fund (ERDF), Grant Number AYUD/2021/57246. The authors would like to thank SEGAI-ULL for assistance with the XRD and TEM measurements.

## References

- 1 D. G. Nocera, *Acc. Chem. Res.*, 2012, **45**, 767.
- 2 J. P. Torella, *et al.*, *Proc. Natl. Acad. Sci. U. S. A.*, 2015, **112**, 2337.
- 3 L. Wondraczek, E. Tyystjärvi, J. Méndez-Ramos, F. A. Müller and Q. Zhang, *Adv. Sci.*, 2015, **2**, 1500218.
- 4 J. Méndez-Ramos, P. Acosta-Mora, J. C. Ruiz-Morales, T. Hernández, M. E. Borges and P. Esparza, *RSC Adv.*, 2013, **3**, 23028.
- 5 J. Méndez-Ramos, M. E. Borges, S. Torres-García, M. Medina-Alayón, P. Acosta-Mora, J. del-Castillo, A. Menéndez-Velázquez, C. B. Mullins and P. Esparza, *J. Power Sources*, 2025, **625**, 235668.
- 6 J. de Wild, A. Meijerink, J. K. Rath, W. G. J. H. M. van Sark and R. E. I. Schropp, *Energy Environ. Sci.*, 2011, **4**, 4835.
- 7 A. Fujishima and K. Honda, *Nature*, 1972, **238**, 37.
- 8 P. Acosta-Mora, K. Domen, T. Hisatomi, H. Lyu, J. Méndez-Ramos, J. C. Ruiz-Morales and N. M. Khaidukov, *Chem. Commun.*, 2018, **54**, 1905.
- 9 D. K. Bora, A. Braun and E. C. Constable, *Energy Environ. Sci.*, 2013, **6**, 407.
- 10 Y. Lin, G. Yuan, S. Sheehan, S. Zhou and y. D. Wang, *Energy Environ. Sci.*, 2011, **4**(12), 4862.
- 11 H. Liu, X. Fan, Y. Li, H. Guo, W. Jiang and y G. Liu, *J. Environ. Chem. Eng.*, 2023, **11**(1), 109224.
- 12 K. Sivula, F. Le Formal and y. M. Grätzel, *ChemSusChem*, 2011, **4**(4), 432.
- 13 F. Gonell, M. Haro, R. S. Sánchez, P. Negro, I. Mora-Seró, J. Bisquert, B. Julián-López and S. Giménez, *J. Phys. Chem. C*, 2014, **118**(21), 11279.
- 14 C. Pornrungrroj, V. Andrei and E. Reisner, *J. Am. Chem. Soc.*, 2023, **145**(25), 13709.
- 15 J. Méndez-Ramos, J. C. Ruiz-Morales, P. Acosta-Mora, J. del-Castillo and A. C. Yanes, *J. Power Sources*, 2013, **238**, 313.
- 16 M. Zhang, Y. Lin, T. J. Mullen, W.-F. Lin, L.-D. Sun, C.-H. Yan, T. E. Patten, D. Wang, G.-Y. Liu and J. Phys, *Chem. Lett.*, 2012, **3**(21), 3188.
- 17 M. E. Borges, H. de Paz Carmona, M. Gutiérrez and P. Esparza, *Catalysts*, 2023, **13**(6), 1023.
- 18 S. P. Sahu, S. I. Cates, H.-I. Kim, J.-H. J. Kim and E. L. Cates, *Environ. Sci. Technol.*, 2018, **52**, 2973.
- 19 J. Wang, R. Li, Z. Zhang, W. Sun, R. Xu, Y. Xie, Z. Xing and X. Zhang, *Appl. Catal., A*, 2008, **334**, 227.
- 20 J. Wang, Y. Xie, Z. Zhang, J. Li, X. Chen, L. Zhang, R. Xu and X. Zhang, *Sol. Energy Mater. Sol. Cells*, 2009, **93**, 355.
- 21 J. del-Castillo, J. Méndez-Ramos, P. Acosta-Mora and A. C. Yanes, *J. Lumin.*, 2022, **241**, 118490.
- 22 K. Aitola, G. Gava Sonai, M. Markkanen, J. Kaschuk, X. Hou, K. Miettunen and K., P. D. Lund, *Sol. Energy*, 2022, **237**, 264.
- 23 A. B. García-Delgado, A. Menéndez-Velázquez, J. Méndez-Ramos, S. Torres-García, M. Medina-Alayón, P. Acosta-Mora, J. del-Castillo, M. E. Borges and P. Esparza, *J. Lumin.*, 2024, **273**, 120671.



- 24 L. Vayssieres, J. Guo and J. Nordgren, *J. Nanosci. Nanotechnol.*, 2001, **1**, 385.
- 25 J. Mathew and N. Nirmala, *Int. J. Appl. Bioeng.*, 2015, **9**, 36.
- 26 C. M. S. Jones, N. Panov, A. Skripka, J. Gibbons, F. Hesse, J.-W. G. Bos, X. Wang, F. Vetrone, G. Chen, E. Hemmer, *et al.*, *Opt. Express*, 2020, **28**, 22803.
- 27 B. Chen and F. Wang, *Acc. Chem. Res.*, 2020, **53**, 358.
- 28 Z. Wang and A. Meijerink, *J. Phys. Chem. C*, 2018, **122**, 26298.
- 29 S. Liu and Y.-J. Xu, *Sci. Rep.*, 2016, **6**, 22742.
- 30 J. C. Myland and K. B. Oldham, *Electrochem. Commun.*, 2004, **6**(4), 344.
- 31 A. Santana-Alonso, A. C. Yanes, J. Méndez-Ramos, J. del-Castillo and V. D. Rodríguez, *Opt. Mater.*, 2011, **33**, 587.

